# Assessment of myocardial elastography performance in phantoms under combined physiologic motion configurations with preliminary *in vivo* feasibility



2012 Phys. Med. Biol. 57 5633

(http://iopscience.iop.org/0031-9155/57/17/5633)

IOP PUBLISHING PHYSICS IN MEDICINE AND BIOLOGY

Phys. Med. Biol. **57** (2012) 5633–5650 doi:10.1088/0031-9155/57/17/5633

# Assessment of myocardial elastography performance in phantoms under combined physiologic motion configurations with preliminary *in vivo* feasibility

**S J Okrasinski**[1], **B Ramachandran**[1] **and E E Konofagou**[1,2]

[1] Department of Biomedical Engineering, Columbia University, 622 West 168th St., Vanderbilt Clinic, New York, NY 10032, USA

[2] Department of Radiology, Columbia University, 622 West 168th St., Vanderbilt Clinic, New York, NY 10032, USA

E-mail: ek2191@columbia.edu

Received 30 March 2012, in final form 20 June 2012

Published 14 August 2012

Online at stacks.iop.org/PMB/57/5633

**Abstract**

Myocardial elastography (ME) is a non-invasive, ultrasound-based strain imaging technique, which can detect and localize abnormalities in myocardial function. By acquiring radio-frequency (RF) frames at high frame rates, the deformation of the myocardium can be estimated, and used to identify regions of abnormal deformation indicative of cardiovascular disease. In this study, the primary objective is to evaluate the effect of torsion on the performance of ME, while the secondary objective is to image inclusions during different motion schemes. Finally, the phantom findings are validated with an *in vivo* human case. Phantoms of homogeneous stiffness, or containing harder inclusions, were fixed to a pump and motors, and imaged. Incremental displacements were estimated from the RF signals, and accumulated over a motion cycle, and rotation angle, radial strain and circumferential strain were estimated. Phantoms were subjected to four motion schemes: rotation, torsion, deformation, and a combination of torsion and deformation. Sonomicrometry was used as a gold standard during deformation and combined motion schemes. In the rotation scheme, the input and estimated rotation angle agree in both the homogeneous and inclusion phantoms. In the torsion scheme, the estimated rotation angle was found to be highest, closest to the source of torsion and lowest farthest from the source of torsion. In the deformation scheme, if an inclusion was not present, the estimated strain patterns accurately depicted homogeneity, while if an inclusion was present, abnormalities were observed which enabled detection of the inclusion. In addition, no significant rotation was detected. In the combined scheme, if an inclusion was not present, the estimated strain patterns accurately depicted homogeneity, while, if an inclusion was present, abnormalities were observed which enabled detection of the inclusion. Also, torsion was separated from the combined scheme and was found to be similar to the pure torsion findings. This study shows ME to be capable of accurately depicting and distinguishing between different types of motion schemes, and to be sensitive to stiffness changes in localized regions of tissue-mimicking phantoms under physiologic cardiac motion configurations, while strains estimated in the combined motion scheme were noisier than in individual motion schemes. Finally, ME was shown to be capable of distinguishing between deformation and rotation in a normal human heart *in vivo*.

(Some figures may appear in colour only in the online journal)

## 1. Introduction

In order to provide timely treatment to patients suffering from cardiac disease, early diagnosis is the key. Cardiac motion is a combination of several different physiologic motion types, most notably translation, rotation, torsion, and deformation. Cardiac torsion is usually estimated as the difference between counter-clockwise basal and clockwise apical rotation, and has been studied in several different pathologies. Depending on the condition, torsion has been found to both increase and decrease, e.g., it has been observed that peak left-ventricular torsion is reduced in human subjects as a result of cardiac ischemia (Bansal *et al* 2008) and myocardial infarction (Govind *et al* 2010), while it is increased in patients with diabetes mellitus (Shivu *et al* 2009). In addition, deformation has been previously studied as a diagnostic factor for pathologies such as ischemia (Hashima *et al* 1993, Villarreal *et al* 1991) and infarction (Götte *et al* 2001). In the healthy myocardium, positive radial thickening and negative circumferential shortening are expected throughout the myocardium, while in ischemia and infarction strain reduction has been observed. With a relationship established between these cardiac pathologies and changes in left-ventricular motion, a technique to estimate cardiac strain and torsion could help clinicians diagnose such strain-altering pathologies.

Several groups have explored the use of cardiac motion estimation algorithms in order to estimate strains. Tissue Doppler imaging (TDI) (Hoffman *et al* 2002, Miyatake *et al* 1995, Sutherland *et al* 1994) is a technique, which uses Doppler-based techniques to estimate myocardial motion. This technique has also been expanded to provide strain estimation (Edvardsen *et al* 2001). As these techniques are Doppler-based, they suffer from the Doppler-associated angle dependence and aliasing. Strain rate imaging (SRI) is a technique, which was originally based on TDI (Heimdal *et al* 1998), but later overcame the Doppler-associated angle dependence by estimating motion using time-domain techniques (D'hooge *et al* 2002). Optical flow (Duan *et al* 2006, Sühling *et al* 2004, Mailloux *et al* 1987, Meunier *et al* 1987, 1998) estimates motion by observing changes in brightness over space and time, and have been shown to accurately estimate motion in simulations and *in vivo* (Mailloux *et al* 1987). Registration-based methods (Papademetris *et al* 2001, Ledesma-Carbayo *et al* 2005, Elen *et al* 2008) estimate motion by registering successive ultrasound frames with a deformable shape-tracking approach. Strain imaging techniques have been developed in previous studies (Kaluzynski *et al* 2001, Varghese *et al* 2003, Langeland *et al* 2004, Lopata *et al* 2009). In these techniques, a reference kernel in a pre-deformation image is matched to a region in a post-deformation image.

Myocardial elastography (ME) (Lee *et al* 2007, Konofagou *et al* 2000), an angle-independent (Zervantonakis *et al* 2007, Lee and Konofagou 2008), radio-frequency (RF)-based technique, was developed to map the 2D transmural deformation field and detect abnormal cardiac function (Lee *et al* 2008, 2011). ME has been validated against sonomicrometry in canines (Lee *et al* 2011) and MR tagging in humans (Lee *et al* 2008) *in vivo*. During the cardiac cycle, the myocardium undergoes a combination of motion components including torsion, deformation, and translation. In order to assess influence of each motion component on the results of ME, it is necessary to compare against a ground truth in a setup which allows control over the motion components, which, in an *in vivo* setting, is rarely possible. An experimental phantom setup can be used to test the performance of the estimated strains and torsion.

Several cardiac phantoms have been developed in previously reported studies in order to validate speckle tracking techniques. The phantom developed by Ashraf *et al* (2006) includes a freshly harvested pig heart mounted on a motor used to induce rotation and torsion. While this technique was capable of simulating torsion, the combination study of radial deformation and torsion was not studied.

Several groups (Kaluzynski *et al* 2001, Langeland *et al* 2004, Ribbers *et al* 2007) have reported cylindrical phantoms in an external radial deformation configuration. In two of these models (Kaluzynski *et al* 2001, Langeland *et al* 2004), stiffer regions were included into a portion of the wall of the phantom in order to study strains in the presence of a stiff lesion. Strains were tracked as a pump-induced deformation in the radial and circumferential principal directions. Smith and Rinaldi (1989), Jia *et al* (2006) and Lesniak-Plewinska *et al* (2010) report phantoms with a geometry which was intended to mimic more closely the geometry of the heart. Similarly, strains were estimated during pump-induced radial deformation (Jia *et al* 2006), but the combined effects of deformation and torsion were not examined.

To the knowledge of the authors, no previous study has been reported, which simultaneously mimicked more complex motion, i.e. combined torsion and deformation, in a phantom for assessing the performance of RF-based speckle tracking. Understanding the interaction between these motion components is critical for interpreting results *in vivo*, where these and other motion components are coupled.

In this study, we aimed at the evaluation of the influence of rotation, torsion, and deformation motion schemes, separately or in combination, on the results of ME by using non-inclusion and inclusion phantoms (Gamarnik *et al* 2007), and confirmed the findings in an *in vivo* human case. Ultrasound RF frames were acquired, and 2D, including angular, displacements were estimated under rotation, torsion, deformation, and combined motion configurations.

## 2. Materials and methods

### *2.1. Phantom design*

Polyacrylamide (Acros Organics, Geel, Belgium) gel phantoms were used to model the left ventricle of the human heart. The cylindrical phantom (figure 1) was molded as a thick-walled, hollow cylinder in order to mimic the geometry of the left ventricle in the short-axis view, and the center was left hollow to allow water to flow through the phantom and cause wall motion and deformation. The phantom was 15 cm long with an outer diameter of 24.5 mm and a wall thickness of 7.5 mm. Two phantoms were prepared for this study: one of uniform wall stiffness (non-inclusion) and one containing a stiff inclusion representing a region of reduced compliance. The phantoms had a wall stiffness of 25 kPa, while the inclusion had a stiffness of 50 kPa. The inclusion measured 25 mm in length, 7.5 mm in thickness, extended 90 degrees around the phantom, and was located at the center of the length of the phantom.

To achieve a 25 kPa and 50 kPa stiffness, 30% and 40% concentrations of polyacrylamide were used, respectively. These concentrations have been previously shown to produce the indicated stiffnesses (Maleke *et al* 2007). This relationship between the concentration of polyacrylamide and stiffness was verified using mechanical testing. Agar was added to the

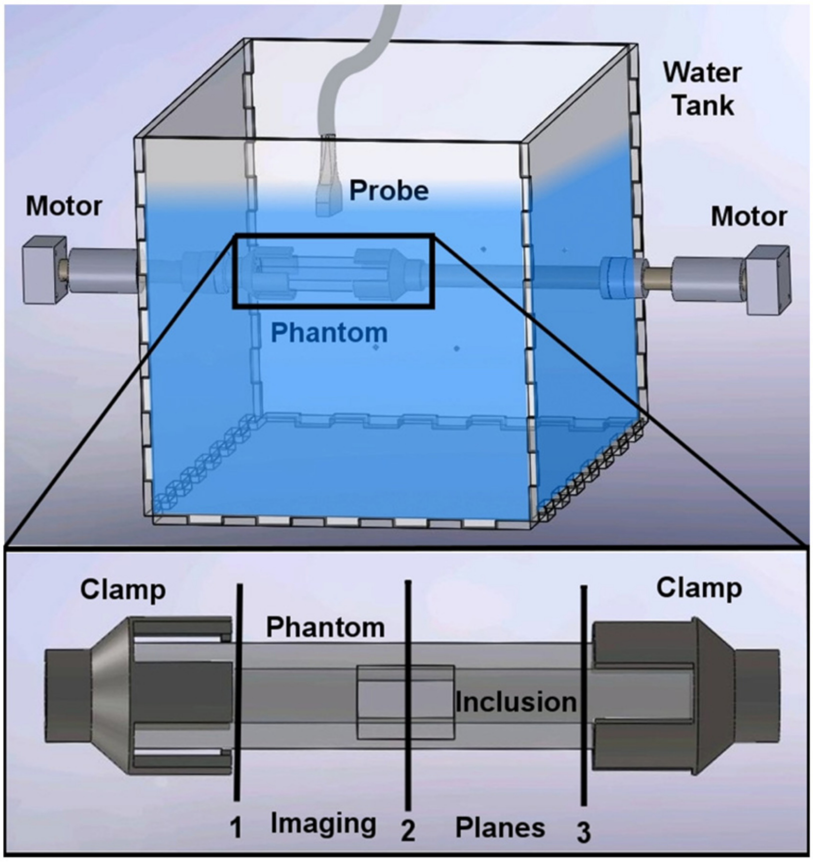


**Figure 1.** Experimental setup used to impose motion schemes on a phantom. Motors are used to impose rotation and torsion, while a pump is used to induce deformation. The inflow and outflow of the pump are attached to the left and right aluminum tubes, respectively. The inclusion phantom mounted on clamps and immersed in degassed water (blue shade), with the stiff inclusion located in the center, is shown in the detail window. The three transverse imaging planes considered in this study are indicated.

polyacrylamide in order to enhance scattering (34.9 mg per ml) prior to gel polymerization. The solution was well mixed, poured into a custom mold, and stored in a refrigerated water bath for 24 h to allow the polyacrylamide to fully polymerize. In order to construct a phantom with a stiff inclusion, a phantom with a stiffness of 50 kPa was first built. The inclusion was cut from this initial phantom, and was placed in the phantom mold. The 30% polyacrylamide solution was then poured into the mold. As the polyacrylamide gelled, it bonded with the inclusion, forming a 25 kPa body with a well-bonded 50 kPa inclusion. When not in use, the phantoms were returned to a refrigerated water bath in order to preserve its original stiffness.

### 2.2. Experimental setup

An experimental setup was designed and built to apply predefined motion schemes to the phantoms (figure 1). An acrylic tank was built to contain the phantom surrounded by a degassed water volume. Aluminum pipes were passed through the walls of the tank. Thrust bearings were used with shaft collars to ensure that the pipes were well anchored and able to rotate easily.

The phantom was fixed to the ends of both pipes with a custom-made compressional fitting. The pipes were connected to a peristaltic pump (Manostat, Barrington, IL), allowing water to circulate through the phantom. As the pump circulated water, the flow caused the phantom to expand and relax in similar directions as the expansion and contraction of the left ventricle in the short-axis view. The pumping frequency was chosen to be 1 Hz, as this rate is similar to a healthy heart rate, and this frequency produced maximal deformation in the phantom, which was assessed by inspection of the B-mode ciné loops. Computer-controlled stepper motors were mounted to both aluminum pipes. This configuration allowed the phantom to be subjected to rotation and torsion via the stepper motors, and deformation via the peristaltic pump, separately or simultaneously as needed. Rubber absorbers were placed along the wall of the tank in order to reduce acoustic reflections.

### *2.3. Sonomicrometry*

A total of four piezoelectric crystals (Sonometrics Corp., London, Ontario, Canada) were placed on the phantom, and the distance between all crystal pairs was continuously monitored. The four piezoelectric crystals were thus positioned in a tetrahedral configuration in the center of the phantom. The average separation of the tetrahedral crystals was equal to 8 mm. One crystal was implanted immediately beneath the inner wall of the phantom, while the remaining three crystals were inserted in the outer wall of the phantom. Ten-second long sonomicrometry data acquisitions at a sampling rate of 379 Hz were acquired during each motion configuration, and acquisition occurred after RF capture. The regional strain was calculated in cardiac coordinates based on the shape change of the crystal tetrahedron. Sonomicrometry data analysis has been previously described in detail (Lee *et al* 2011). Briefly, the distance between crystals is measured by the time of flight of an acoustic signal from one crystal to the others. This distance can then be used to estimate strain.

### *2.4. Data acquisition*

A SonixTOUCH (Ultrasonix Medical Corp., Richmond, BC, Canada) ultrasound system equipped with a 5 MHz, 128-element linear array transducer (L14–5) was used to acquire RF signals. These signals were acquired using 128-beam density, 8 cm depth, and 20 MHz sampling frequency. The phantom did not fill the entire width of the full view, so the sector size was changed to 60%. As a result, 76 beams were recorded. The resulting frame rate was 187 fps. For each set of RF frames, at least three repetitions (i.e. an approximate total time of 3 s) of each motion scheme were recorded and stored for offline processing.

Four separate motion schemes were applied to the phantom:

(1) Rotation was applied by rotating the stepper motors on each end of the phantom in both clockwise and counterclockwise directions. Each motor rotated 30 degrees at a speed of 112 degrees per second. These rotation parameters were chosen to mimic the rotation rate and degree in the normal human heart (Carreras *et al* 2011). RF frames were acquired in three distinct locations: through the center of the phantom, and 5 cm towards the left or right edge of the phantom, as shown in figure 1.
(2) Torsion was applied to the phantom by rotating one stepper motor and maintaining the other motor fixed. One motor rotated for 30 degrees clockwise at a speed of 112 degrees per second (268 ms) while maintaining the second motor fixed, and then paused for 732 ms. Then, the same motor rotated at the same speed for 30 degrees in the counter-clockwise direction. The applied torsion was $2.3^\circ$ cm$^{-1}$. RF frames were acquired from all three imaging planes (figure 1) under separate renditions of the same motion pattern.

(3) Deformation was applied to the phantom by using the peristaltic pump. As the pump circulated water through the lumen of the phantom, the pulsatile flow induced by the pump caused the phantom to expand radially and shorten circumferentially, analogous to the principal directions of deformation in the short-axis view in a human heart. RF frames were acquired in one location (plane 2) in order to compare the strains estimated in the non-inclusion and inclusion cases.
In this paper, the term 'relaxation' is used to describe the deformation phase when the phantom transitions from an expanded to unexpanded state. Note that 'relaxation' is used differently from the *in vivo* cardiac terminology.
(4) A combination of torsion and deformation was studied. The pumping frequency was equal to 1 pulse per second, and the motor inducing rotation was synchronized to start its clockwise rotation at the beginning of the pump stroke. One motor rotated for 30 degrees clockwise at a speed of 112 degrees per second (268 ms) while maintaining the second motor fixed, and then paused for 732 ms. Then, the same motor rotated at the same speed for 30 degrees in the counter-clockwise direction, and a new pump pulse was initiated. This timing was selected to ensure that the deformation caused by the pump was synchronized with the deformation caused by the motor. RF frames were acquired within a single plane (plane 2) in order to compare deformation and torsion estimates.

These motion schemes were selected because rotation, torsion, and deformation are the primary components of cardiac motion that occur in unison in both healthy and pathological hearts while being altered in the latter. In order to understand how ME estimates and eventually distinguishes between a complex combination of these motion types, it is important to understand how these individual components are estimated, and how these estimates vary under pathological conditions. A combination of the components was also studied in order to determine how torsion and strain can be estimated when both occur simultaneously, similar to the *in vivo* case. While the strain magnitudes and torsion rates in this study are not necessarily representative of the physiological values, the objective of this study was nevertheless met, i.e. the performance of ME could be assessed in the presence of each motion scheme or combination thereof.

### *2.5. Myocardial elastography*

Two-dimensional, in-plane orthogonal (lateral and axial) displacement components were estimated using one-dimensional (1D) normalized cross-correlation and re-correlation techniques in a 2D search previously described elsewhere (Konofagou and Ophir 1998, Lee *et al* 2007, Fung-Kee-Fung *et al* 2005). Briefly, the cross-correlation technique employed a 1D matching kernel of 4.6 mm and 90% overlap. The reference and comparison frames comprised the RF signals before and after motion, respectively. The RF signal segment in the comparison frame corresponding to the maximum cross-correlation value was considered to be the best match to the RF signal segment in the reference frame. Cosine interpolation was then applied around the peak of the cross-correlation function for a more refined peak search (Konofagou *et al* 2002). Thus, the lateral and axial shifts between the reference and comparison RF segments with the highest cross-correlation peak value denoted the lateral and axial displacements, respectively. A correction (or, recorrelation) in the axial displacement estimation was performed to reduce the decorrelation resulting from lateral motion. It was implemented by shifting RF signal segments by the estimated axial displacement in the comparison frame, prior to the second lateral displacement estimation. Likewise, a recorrelation in the lateral displacement estimation was performed to reduce the decorrelation resulting from axial motion. The incremental 2D displacements that occurred from the beginning to the end of the applied motion were then integrated to obtain the cumulative 2D displacement. For each pixel, appropriate registration between consecutive displacement images was performed in order to ensure that the cumulative displacement depicted the motion in the same phantom region.

Cumulative 2D (i.e. lateral and axial) Lagrangian finite strains were derived from the cumulative 2D displacements (Lee *et al* 2007). Positive and negative 2D strains indicated tension and compression, respectively. In ME, a least-squares strain estimator (LSQSE) (Kallel and Ophir 1997) with a kernel of 3.7 mm in both the lateral and axial directions was used in order to improve the signal-to-noise ratio (SNR) of the strain image. The aforementioned 2D finite strains are dependent on the orientation of the ultrasound transducer relative to the phantom (Zervantonakis *et al* 2007). Therefore, polar (i.e. radial and circumferential) strains were additionally obtained by defining an angle with respect to the centroid of the phantom and through coordinate transformation of the finite strain. Likewise, angular displacement was obtained by applying a coordinate transform using the centroid defined above. Torsion was estimated by subtracting rotation in plane 3 from rotation in plane 1, divided by the distance, 13 cm. Positive and negative radial strains indicated wall thickening and thinning, respectively, while wall stretching and shortening were represented by positive and negative circumferential strains, respectively.

Uncertainties reported for rotation and torsion quantities are the standard deviation of the estimates across a single imaging plane, while uncertainties reported for deformations are the standard deviation of strain in the phantom sector from 11 o'clock to 1 o'clock in a single imaging plane.

### *2.6. In vivo human subject*

One healthy, 24-year-old male was scanned for *in vivo* feasibility of the methodology. The subject was consented under a study approved by the Columbia University's institutional review board. Short axis views at the level of the papillary muscle were found by a cardiologist, and RF signals were acquired using a Sonix MDP (Ultrasonix Medical Corp., Richmond, BC, Canada) ultrasound system equipped with a 3.3 MHz, 128-element phased array transducer (P4–2). A sector-based imaging technique was used (Wang *et al* 2008) in order to achieve a frame rate of 198 fps. Five sectors were used, and the full-view cine loop was reconstructed using a total of ten consecutive cardiac cycles. Cumulative radial strain and rotation at the end of systole in a short-axis at the mid left-ventricular level was estimated from the same data set.

## 3. Results

Both non-inclusion and inclusion phantoms were subjected to the four motion configurations detailed in the previous section, and displacements and strains were estimated. The results are outlined below separately for each motion scheme.

### *3.1. Rotation scheme*

The estimated angular displacements from plane 2 during rotation are shown in figure 2. Figure 3 summarizes average ROI values from 11 to 1 o'clock. It shows that the rotation angles in the non-inclusion phantom were $28 \pm 4^\circ$, $27 \pm 2^\circ$, and $29 \pm 3^\circ$ in planes 1, 2, and 3, respectively (figure 3). In the inclusion phantom, the rotation angles were $29 \pm 6^\circ$, $30 \pm 5^\circ$, and $29 \pm 3^\circ$. Within each phantom, the rotation angle estimates were in agreement

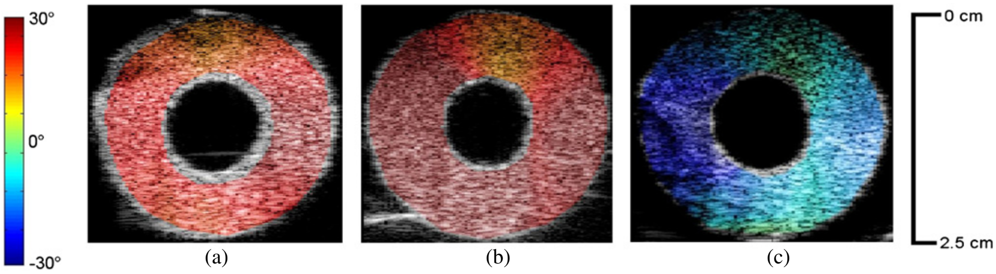


**Figure 2.** Peak clockwise rotation in (a) non-inclusion and (b) inclusion phantoms and peak counter-clockwise rotation in the (c) non-inclusion phantom in plane 2. The rotation was uniform along different slices in both phantoms.

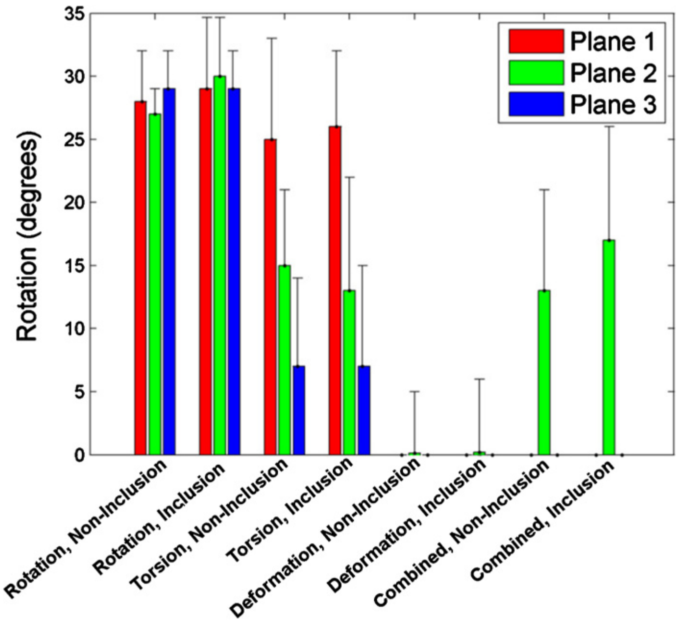


**Figure 3.** Estimated peak rotation in different motion schemes. Rotation measurements were not made in planes 1 and 3 in the deformation and combined scheme.

across planes 1, 2, and 3. In addition, the results from the inclusion and non-inclusion phantoms were very similar, indicating that ME detected similar rotation inside and outside of the stiff inclusion. Finally, note that the rotation angle and direction ($-28 \pm 6°$) were also accurately detected when the phantom was undergoing counter-clockwise rotation (figure 2(c)).

### *3.2. Torsion scheme*

The estimated angular displacements during torsion (figures 4 and 5) are shown. Average values from an ROI at 12 o'clock (figure 3) show that the rotation angles in the non-inclusion phantom were $25 \pm 8°$, $15 \pm 6°$, and $7 \pm 7°$ in planes 1, 2, and 3, respectively. In the inclusion phantom, the rotation angles were $26 \pm 6°$, $13 \pm 9°$, and $7 \pm 8°$. These estimated

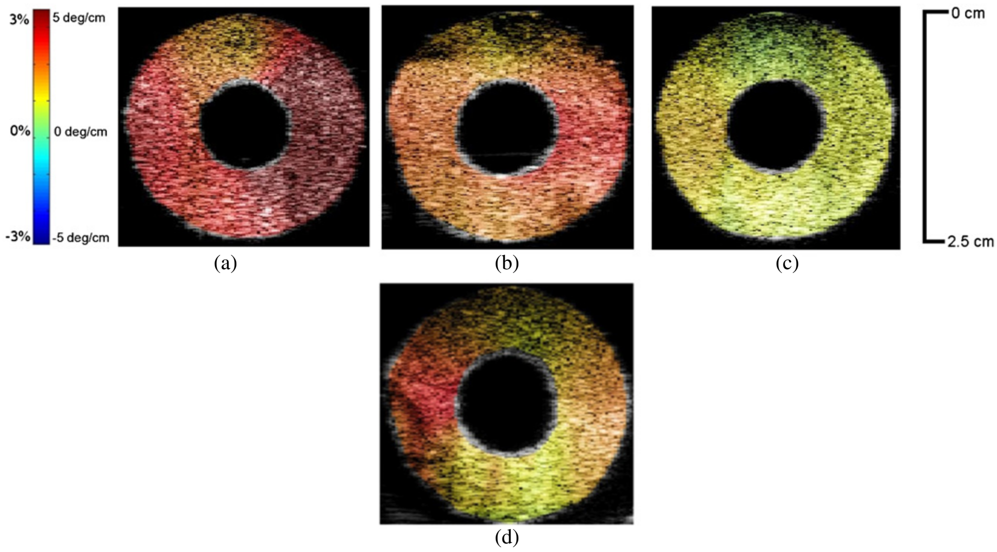


**Figure 4.** Peak angular displacement during clockwise torsion in a non-inclusion phantom in (a) plane 1, (b) plane 2, and (c) plane 3, and the resulting (d) torsion. Note the gradient from the rotating to the fixed end.

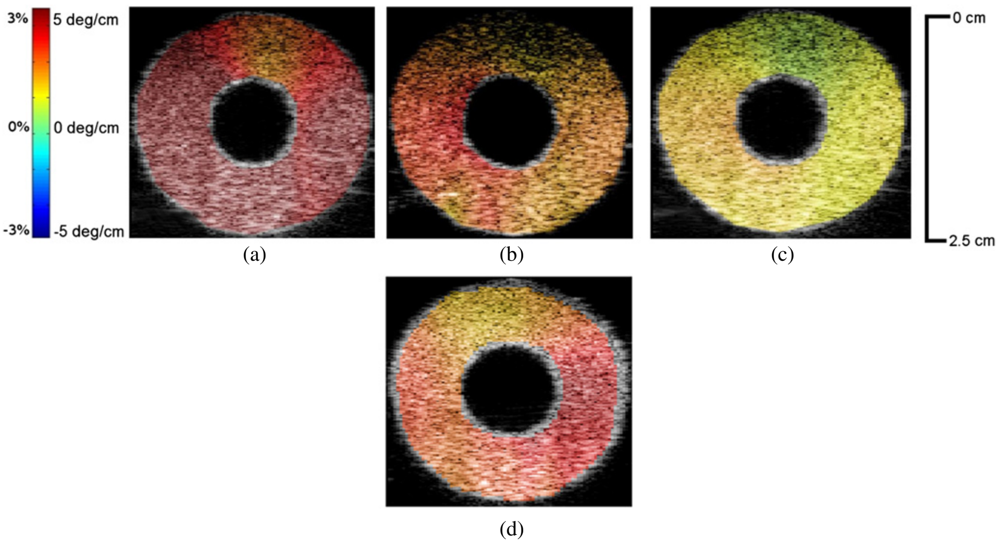


**Figure 5.** Peak angular displacement during clockwise torsion in an inclusion phantom in (a) plane 1, (b) plane 2, and (c) plane 3, and the resulting (d) torsion. No outline of the stiff inclusion is observable.

rotations indicate that the largest rotation angle is closest to the rotational source as expected. The estimated torsion in each phantom was $2.2 \pm 1^{\circ}$ cm$^{-1}$ and $2.4 \pm 1^{\circ}$ cm$^{-1}$ in the non-inclusion and inclusion phantoms, respectively. In addition, the torsion is similar between non-inclusion and inclusion phantoms.

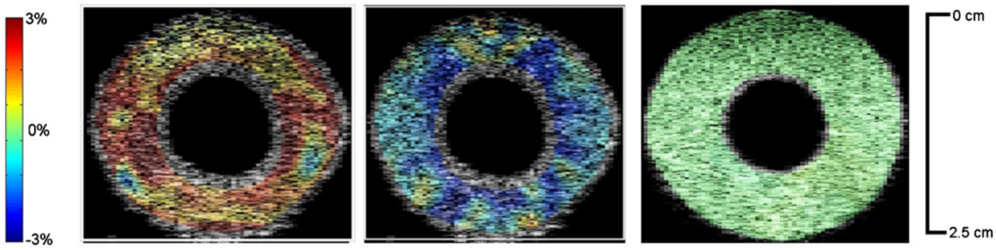


**Figure 6.** Peak cumulative (a) radial and (b) circumferential strain and (c) rotation during relaxation in a non-inclusion phantom. Note the uniform radial and circumferential strain, indicative of uniform wall stiffness.

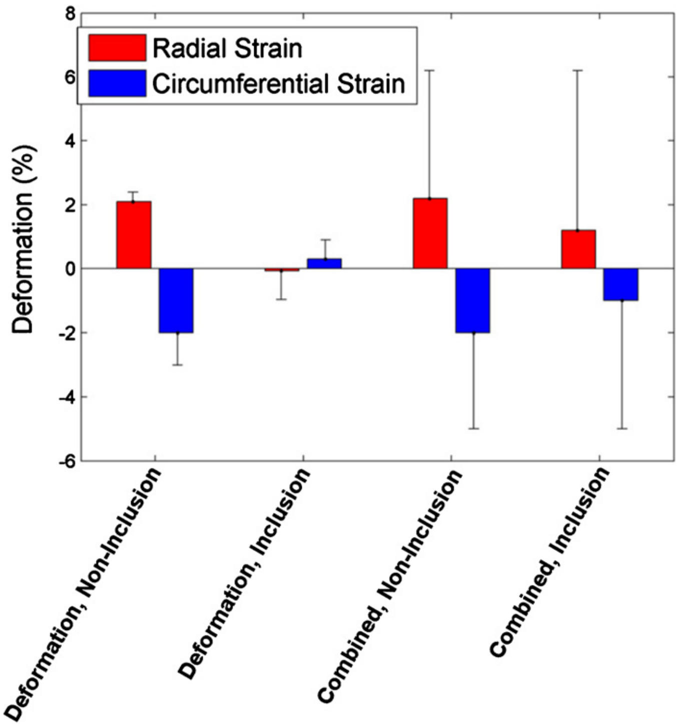


**Figure 7.** Estimated deformation in different motion schemes.

### *3.3. Deformation scheme*

During relaxation in the non-inclusion phantom (figure 6), radial thickening and circumferential shortening can be observed. The deformation was averaged in a region of interest extending from 11 to 1 o'clock, and the average peak radial and circumferential strains were found to be equal to 2.1 $\pm$ 0.3% and $-2.0$ $\pm$ 1%, respectively (figure 7). During relaxation in the inclusion phantom (figure 8), there is an area of reduced strain from 10 to 2 o'clock, indicating lower magnitude of radial thickening and circumferential shortening. When the strains were averaged in the region of the inclusion, average peak radial and circumferential strains were found to be equal to $-0.07$ $\pm$ 0.9% and 0.3 $\pm$ 0.6%, respectively (figure 7).

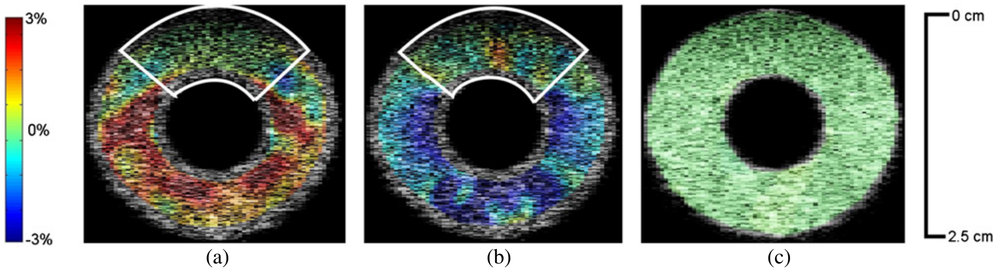


**Figure 8.** Peak cumulative (a) radial and (b) circumferential strain and (c) peak rotation during relaxation in an inclusion phantom. The inclusion is outlined in white. Note the regions of reduced strains within the region of the inclusion.

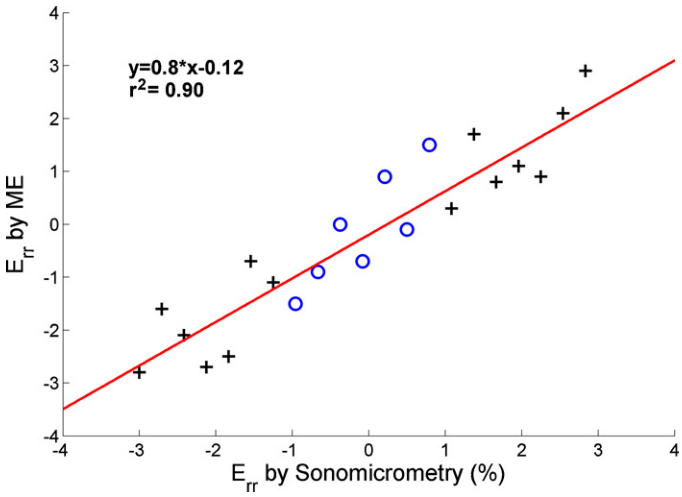


**Figure 9.** A scatter plot of the radial strain ($E_{rr}$) estimated from ME and sonomicrometry. A blue 'o' indicates an ME strain estimate from an inclusion phantom, while a black '+'indicates an ME strain estimate from a non-inclusion phantom.

These lower-magnitude strains were observed from 10 to 2 o'clock, which is where the stiff inclusion was located, and the size of the strain reduction agrees with the size of the inclusion. Also, the estimated rotation angles in the center plane (figures 6 and 8) were $2 \pm 5°$ and $-1 \pm 6°$ for the non-inclusion and inclusion phantom, respectively.

A comparison was performed between strains estimated from ME and sonomicrometry. Radial and circumferential strain comparisons are shown in figures 9 and 10, respectively. A good correlation was found for both radial and circumferential strains ($r^2 = 0.90$ and 0.71, respectively).

### 3.4. Combination scheme

During relaxation in the non-inclusion phantom (figure 11), radial thickening, circumferential thinning, and clockwise angular displacement can be observed. The deformation was averaged in a region of interest, and the average peak radial and circumferential strains were $2.2 \pm 0.5\%$ and $-2.1 \pm 7\%$, respectively, while the torsion was $2.8 \pm 2°\ \mathrm{cm}^{-1}$. During

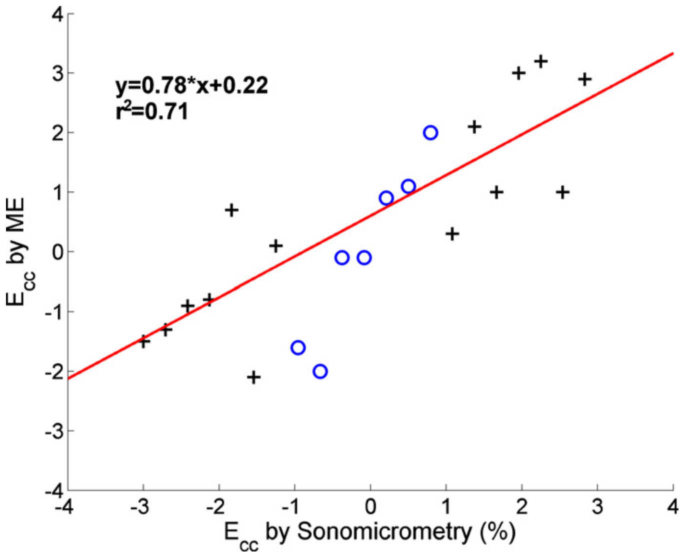


**Figure 10.** A scatter plot of the radial strain ($E_{cc}$) estimated from ME and sonomicrometry. A blue 'o' indicates an ME strain estimate from an inclusion phantom, while a black '+'indicates an ME strain estimate from a non-inclusion phantom.

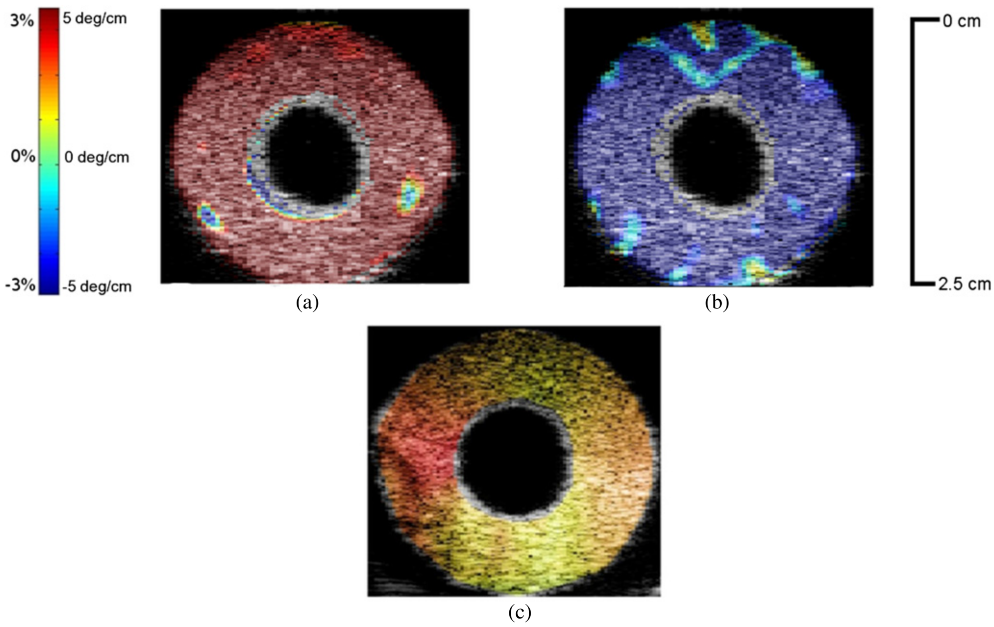


**Figure 11.** Peak cumulative (a) radial strain, (b) circumferential strain, and (c) torsion in a non-inclusion phantom during the combined motion scheme.

relaxation in the inclusion phantom (figure 12), a region of reduced strain from 10 to 2 o'clock was detected, indicating lower magnitude of radial thickening and circumferential shortening, though the region contains noisier estimates, indicated by negative radial and positive circumferential strains, than during pure deformation. When the strains and rotation

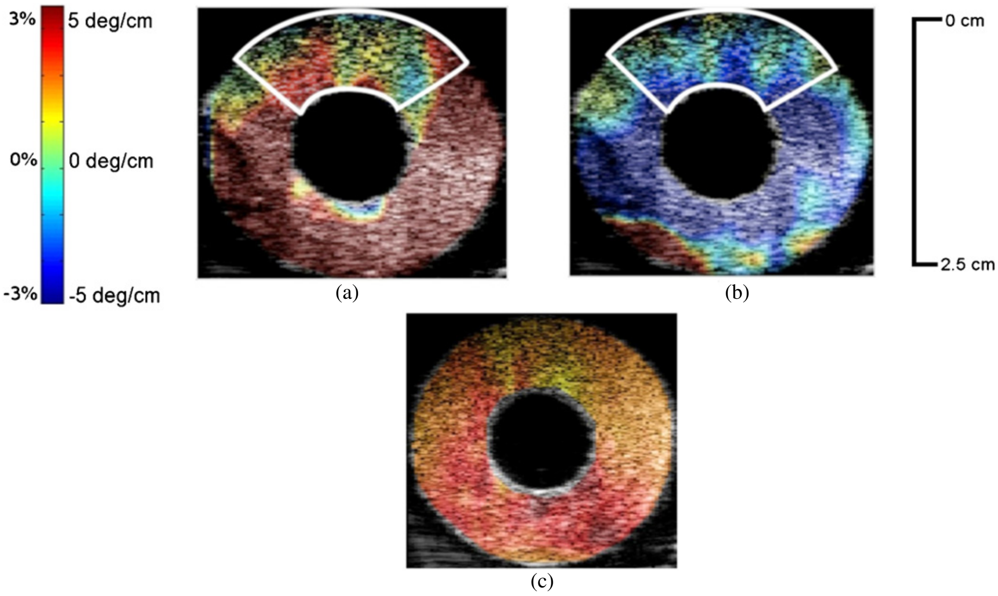


**Figure 12.** Peak cumulative (a) radial strain, (b) circumferential strain, and (c) torsion in an inclusion phantom during the combined motion scheme. Note the regions of reduced strains within the region of the inclusion.

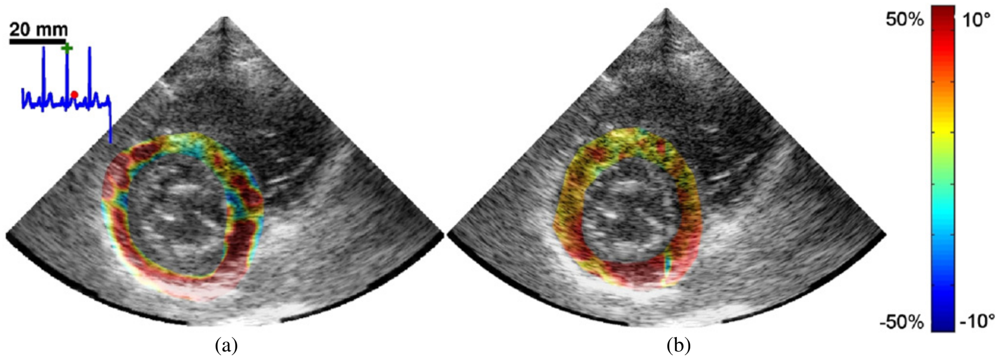


**Figure 13.** Peak cumulative (a) radial strain and (b) rotation at end systole in a normal human subject. Note the uniform strain and rotation, indicative of normal function.

were averaged in the region of the inclusion, average peak radial and circumferential strains were found to be equal to $-1.2 \pm 0.9\%$ and $1 \pm 0.8\%$, respectively, while the torsion was $2.4 \pm 2^\circ$ cm$^{-1}$.

### *3.5. In vivo human subject*

During the systolic phase of the normal heart, the average cumulative radial strain (figure 13(a)) was found to be $37 \pm 10\%$, while the average rotation (figure 13(b)) was found to be $7 \pm 4^\circ$. The radial strain and rotation were simultaneously estimated from a single data set. The uniform radial strain and rotation were observed.

## 4. Discussion

In this study, we aimed at validating ME by using non-inclusion and inclusion left-ventricular phantoms that mimicked the mechanical properties of the myocardium (Gamarnik *et al* 2007). Ultrasound RF frames were acquired, and 2D displacements including angular displacements were estimated under rotation, torsion, deformation, and combined motion configurations. The motion schemes imposed on the phantom were then compared with the ME motion and strain estimates.

In the pure rotation scheme (scheme 1), the estimated and imposed rotation magnitudes and angles were in good agreement, which indicates that ME was capable of accurately depicting rotation in both clockwise and counter-clockwise directions. In both phantoms, the rotation across different slices was consistent (figure 3). Both ends of the phantom were rotated at the same speed and degree, so it was expected that estimations of rotation from planes 1 and 3 would agree. In the case of the inclusion phantom, plane 2, which contained the stiff inclusion, accurately depicted uniform rotation. The inclusion was not detected by a purely rotational scheme, showing that rotation alone was not sufficient to reveal a stiff inclusion in the phantom. As the applied motion is rigid body rotation, this result confirms that we find no evidence of the inclusion with ME.

In the torsion scheme (scheme 2), ME was shown capable of detecting different levels of rotation across the phantom induced by torsion. Again, no significant differences were observed between the non-inclusion and inclusion phantoms (figure 3), showing that torsion alone was not sufficient to reveal a stiff inclusion in the phantom. Again, as this motion is not expected to cause significant strains in the imaging planes considered in this study, this result confirms that we find no evidence of the inclusion with ME. Different degrees of rotation were detected in different planes, showing that ME was capable of distinguishing this motion scheme from pure rotation.

In the rotation and torsion schemes in the phantom, the stiff inclusion was not detected. Note that this result was expected in the phantom, despite it being distinct from the expected clinical result, where stiff infarctions often cause changes in rotation and torsion due to the active contraction of the myocardium (Bansal *et al* 2008).

In the case of deformation, ME was capable of detecting strain in both the non-inclusion and inclusion phantoms. In the non-inclusion phantom, radial and circumferential strains appeared in the expected directions, and their magnitudes (radial: $2.1 \pm 0.3\%$, circumferential: $-2.0 \pm 1\%$) were similar, which is expected due to the known incompressibility of the polyacrylamide (Boudou *et al* 2006). In the inclusion case, the phantom contained a stiff inclusion. The strains estimated in the inclusion were expected to be smaller in magnitude with respect to the non-inclusion phantom. The stiff inclusion can be detected on the radial strain image (figure 8) as reversed radial strain (non-inclusion: $2.1 \pm 0.3\%$, inclusion: $-0.07 \pm 0.9\%$), and in the circumferential image as reversed circumferential strain (non-inclusion: $-2.0 \pm 1\%$, 'inclusion': $0.3 \pm 0.6\%$) at 12 o'clock. The correct extent of the inclusion was also observed on the strain image (figure 8). The rotation was estimated in plane 2, and found to be small (non-inclusion: $2 \pm 5°$ and inclusion: $-1 \pm 6°$), which agreed with the expected lack of rotation. This scheme was then shown to be distinct from rotation and torsion, and was able to detect and demarcate the stiffer inclusion.

In the combined rotation and deformation case, ME was shown capable of detecting consistent torsion in both the non-inclusion and inclusion cases (non-inclusion: $13 \pm 9°$, 'inclusion': $17 \pm 8°$). Strains were found to be different between the non-inclusion and 'inclusion' phantoms in the selected ROI. However, the estimated strains in the two phantoms during the combined motion scheme were noisier, indicated by regions of opposite, or negative radial and positive circumferential, strain, than the estimated strains in the two phantoms during the pure deformation motion scheme. This is likely caused by higher decorrelation noise, and is an important finding of the study since this is more representative to what happens *in vivo*. In the physiological case, where cardiac motion cannot be controlled, it is possible that regions of low stiffness contrast will appear noisy because of this rotation component, as opposed to clear delineation, as expected in stiffer regions (Lee *et al* 2011). In this study, the stiffness of the inclusion was twice that of the phantom (50 and 25 kPa), which represents a slight increase of myocardial stiffness. If the inclusion were stiffer, representing a case closer to an infarction (i.e. 5–10 times stiffer (Mirsky and Parmley 1973)), it is likely that the region would be distinguished at higher strain contrast. This combined scheme is closest to the natural myocardial motion, and provides the closest analog to an *in vivo* case. In this case, expected torsion and deformation patterns were found, though the inclusion region identification was not as distinct as in the pure deformation scheme. Note that although rigid motion was not applied to the phantoms, this model allowed for the study of the effects of torsion on motion and strain estimation, one of the goals of this study.

In the *in vivo* human subject, strain and rotation were estimated simultaneously. The uniform strain and rotation results are indicative of healthy function. In addition, the magnitude of radial strain and rotation are consistent with previous studies. While the particular deformation and torsion magnitudes applied to the phantoms in this study may not have been representative of the physiologic case, the technique was also shown capable of measuring and distinguishing between rotation and deformation in a human subject.

This study was carried out to validate 2D myocardial elastography in non-inclusion and inclusion phantoms and assess its performance under conditions that simulate physiologic motion such as rotation, torsion, and deformation and their combination. Feasibility of the ME technique for measurement of all these schemes was shown by comparing the displacement and strain values obtained from the displacement images during rotation with the applied rotational, torsional, and deformational displacements. Furthermore, the present investigation reproduced the findings in a non-inclusion phantom (Gamarnik *et al* 2007) that the ME technique was previously shown capable of distinguishing between pure rotation and torsion motion. A combined motion configuration and pure rotation or torsion could also be distinguished, and the motion components could be separated in the case of the combined scheme. The reversed radial and circumferential strains in the stiffer region are in excellent agreement with the detection of early onset of ischemia in canines and humans (Lee *et al* 2011). Finally, preliminary *in vivo* results from a human subject are shown, showing *in vivo* feasibility of simultaneous strain and rotation estimation.

As mentioned earlier, the strain magnitude and torsion speed applied to the phantom are not necessarily representative of the physiologic values. In addition, the phantoms constructed in this study represent a passive structure, unlike the actively deforming myocardium. Despite these limitations, the objectives of the study were deemed met, as it was shown possible to investigate the quality of estimation with and without torsion.

## 5. Conclusion

This study showed feasibility of ME in distinguishing between rotation, torsion, and deformation in both decoupled and combined cardiac-mimicking motion schemes. The ME rotation estimates were in excellent agreement with the imposed configurations. The ME torsion estimates were also shown to agree with the input values, and were capable of distinguishing it from rotation. The non-inclusion and inclusion phantoms were successfully differentiated based on the ME strain estimates in the deformation scheme, and shown to be distinct from the rotation scheme. The ME estimates of the combined motion schemes also distinguished the non-inclusion from the inclusion phantoms, and could separately image the torsion from the deformation component, though the strain estimates were noisier in the combined scheme than the pure deformation scheme. Finally, in a preliminary feasibility study, ME was shown capable of distinguishing between rotation and deformation in a normal human heart *in vivo*.

## Acknowledgments

This study was supported by the National Institutes of Health (R01EB00604) and the CTSA program (KL2RR024157). The authors would also like to thank Drs Wei-Ning Lee and Jonathan Vappou for all helpful discussions.

## References

Ashraf M, Li X K, Young M T, Jensen A J, Pemberton J, Hui L, Lysyansky P, Friedman Z, Park B and Sahn D J 2006 Delineation of cardiac twist by a sonographically based 2-dimensional strain analysis method: an in vitro validation study *J. Ultrasound Med.* **25** 1193–8

Bansal M, Leano R L and Marwick T H 2008 Clinical assessment of left ventricular systolic torsion: effects of myocardial infarction and ischemia *Echocardiography* **21** 887–94

Boudou T, Ohayon J, Picart C and Tracqui P 2006 An extended relationship for the characterization of Young's modulus and Poisson's ratio of tunable polyacrylamide gels *Biorheology* **43** 721–28

Carreras F, Garcia-Barnes J, Gil D, Pujadas S, Li C H, Suarez-Arias R, Leta R, Alomar X, Ballester M and Pons-Llado G 2012 Left ventricular torsion and longitudinal shortening: two fundamental components of myocardial mechanics assessed by tagged cine-MRI in normal subjects *Int. J. Cardiovasc. Imaging* **28** 273–84

D'hooge J, Konofagou E, Jamal F, Heimdal A, Barrios L, Bijnens B, Thoen J, Van de Werf F, Sutherland G and Suetens P 2002 Two-dimensional ultrasonic strain rate measurement of the human heart *in vivo IEEE Trans. Ultrason. Ferroelectr. Freq. Control* **49** 281–6

Duan Q, Angelini E D, Gerard O, Homma S and Laine A F 2006 Comparing optical-flow based methods for quantification of myocardial deformations on RT3D ultrasound *IEEE Int. Symp. on Biomed. Imaging* pp 173–6

Edvardsen T, Skulstad H, Aakhus S, Urheim S and Ihlen H 2001 Regional myocardial systolic function during acute myocardial ischemia assessed by strain Doppler echocardiography *J. Am. Coll. Cardiol.* **37** 726–30

Elen A, Choi H F, Loeckx D, Gao H, Claus P, Suetens P, Maes F and D'hooge J 2008 Three-dimensional cardiac strain estimation using spatio-temporal elastic registration of ultrasound images: a feasibility study *IEEE Trans. Med. Imaging* **27** 1580–91

Fung-Kee-Fung S D, Lee W-N, Ingrassia C M, Costa K D and Konofagou E E 2005 Angle-independent strain mapping in myocardial elastography *Proc. IEEE Ultrason. Symp.* pp 516–9

Gamarnik V, Luo J, Lee W-N and Konofagou E E 2007 Experimental assessment of angle-independent myocardial elastography performance using a left-ventricular phantom undergoing physiologic motion *Ultrason. Symp.* pp 741–4

Götte M J, van Rossum A C, Twisk J W R, Kuijer J P A, Marcus J T and Visser C A 2001 Quantification of regional contractile function after infarction: strain analysis superior to wall thickening analysis in discriminating infarct from remote myocardium *J. Am. Coll. Cardiol.* **37** 808–17

Govind S C, Gadiyaram V K, Quintana M, Ramesh S S and Saha S 2010 Study of left ventricular rotation and torsion in the acute phase of ST-elevation myocardial infarction by speckle tracking echocardiography *Echocardiography* **27** 45–9

Hashima A R, Young A A, McCulloch A D and Waldman L K 1993 Nonhomogeneous analysis of epicardial strain distributions during acute myocardial-ischemia in the dog *J. Biomech.* **26** 19–35

Heimdal A, Stoylen A, Torp H and Skjaerpe T 1998 Real-time strain rate imaging of the left ventricle by ultrasound *J. Am. Soc. Echocardiogr.* **11** 1013–9

Hoffmann R, Altiok E, Nowak B, Heussen N, Kuhl H, Kaiser H J, Bull U and Hanrath P 2002 Strain rate measurement by Doppler echocardiography allows improved assessment of myocardial viability in patients with depressed left ventricular function *J. Am. Coll. Cardiol.* **39** 443–9

Jia C, Kim K, Kolias T J, Weitzel W F, Rubin J M and O'Donnell M 2006 P1E-1 left ventricular phantom with pulsatile circulation for ultrasound strain rate imaging *Ultrason. Symp.* pp 1317–20

Kallel F and Ophir J 1997 A least-squares strain estimator for elastography *Ultrason. Imaging* **19** 195–208

Kaluzynski K, Chen X, Emelianov S Y, Skovoroda A R and O'Donnell M 2001 Strain rate imaging using two-dimensional speckle tracking *IEEE Trans. Ultrason. Ferroelectr. Freq. Control* **48** 1111–23

Konofagou E E, D'hooge J and Ophir J 2000 Cardiac elastography—a feasibility study *Proc. IEEE Ultrason. Symp.* pp 1273–76

Konofagou E E, D'hooge J and Ophir J 2002 Myocardial elastography—a feasibility study *in vivo Ultrasound Med. Biol.* **28** 475–82

Konofagou E E and Ophir J 1998 A new elastographic method for estimation and imaging of lateral displacements, lateral strains, corrected axial strains and Poisson's ratios in tissues *Ultrasound Med. Biol.* **24** 1183–99

Langeland S, D'hooge J, Claessens T, Claus P, Verdonck P, Suetens P, Sutherland G R and Bijnens B 2004 RF-based two-dimensional cardiac strain estimation: a validation study in a tissue-mimicking phantom *IEEE Trans. Ultrason. Ferroelectr. Freq. Control* **51** 1537–46

Ledesma-Carbayo M J, Kybic J, Desco M, Santos A, Sühling M, Hunziker P and Unser M 2005 Spatio-temporal nonrigid registration for ultrasound cardiac motion estimation *IEEE Trans. Med. Imaging* **24** 1113–26

Lee W-N, Ingrassia C M, Fung-Kee-Fung S D, Costa K D, Holmes J W and Konofagou E E 2007 Theoretical quality assessment of myocardial elastography with *in vivo* validation *IEEE Trans. Ultrason. Ferroelectr. Freq. Control* **54** 2233–45

Lee W-N and Konofagou E E 2008 Angle-independent and multi-dimensional myocardial elastography—from theory to clinical validation *Ultrasonics* **48** 563–7

Lee W-N, Provost J, Fujikura K, Wang J and Konofagou E E 2011 *In vivo* study of myocardial elastography under graded ischemia conditions *Phys. Med. Biol.* **56** 1155–72

Lee W-N, Qian Z, Tosti C L, Brown T R, Metaxas D N and Konofagou E E 2008 Preliminary validation of angle-independent myocardial elastography using MR tagging in a clinical setting *Ultrasound Med. Biol.* **34** 1980–97

Lesniak-Plewinska B, Cygan S, Kaluzynski K, D'hooge J, Zmigrodzki J, Kowalik E, Kordybach M, Kowalski M and Dual-Chamber A 2010 Thick-walled cardiac phantom for use in cardiac motion and deformation imaging by ultrasound *Ultrasound Med. Biol.* **36** 1145–56

Lopata R, Nillesen M, Hansen H, Gerrits I, Thijssen J and de Korte C 2009 Performance evaluation of methods for two-dimensional displacement and strain estimation using ultrasound radio frequency data *Ultrasound Med. Biol.* **35** 796–812

Mailloux G E, Bleau A, Bertrand M and Petitclerc R 1987 Computer-analysis of heart motion from two-dimensional echocardiograms *IEEE Trans. Biomed. Eng.* **34** 356–64

Maleke C, Luo J and Konofagou E E 2007 2D simulation of the amplitude-modulated harmonic motion imaging (AM-HMI) with experimental validation *IEEE Int. Ultrason. Symp.* pp 797–800

Meunier J, Bertrand M and Mailloux G 1987 A model study of myocardium texture in relation to cardiac dynamics *Ultrason. Imaging* **9** 54–5

Meunier J, Bertrand M, Mailloux G and Petitclerc R 1998 Local myocardial deformation computed from speckle motion *Computers in Cardiology Proc.* pp 133–6

Mirsky I and Parmley W 1973 Assessment of passive elastic stiffness for isolated heart muscle and the intact heart *Circ. Res.* **33** 233–43

Miyatake K, Yamagishi M, Tanaka N, Uematsu M, Yamazaki N, Mine Y, Sano A and Hirama M 1995 New method for evaluating left-ventricular wall-motion by color-coded tissue Doppler imaging: *in vitro* and *in vivo* studies *J. Am. Coll. Cardiol.* **25** 717–24

Papademetris X, Sinusas A J, Dione D P and Duncan J S 2001 Estimation of 3D left ventricular deformation from echocardiography *Med. Image Anal.* **5** 17–28

Ribbers H, Lopata R, Holewijn S, Pasterkamp G, Blankensteijn J and de Korte C 2007 Noninvasive two-dimensional strain imaging of arteries: validation in phantoms and preliminary experience in carotid arteries *in vivo Ultrasound Med. Biol.* **33** 530–40

Shivu G N, Abozguia K, Phan T T, Ahmed I, Weaver R, Narendran P, Stevens M and Frenneaux M 2009 Increased left ventricular torsion in uncomplicated type 1 diabetic patients: the role of coronary microvascular function *Diabetes Care* **23** 1710–2

Smith S W and Rinaldi J E 1989 Anthropomorphic cardiac ultrasound phantom *Ultrason. Symp.* pp 931–4

Sühling M, Jansen C, Arigovindan M, Buser P, Marsch S, Unser M and Hunziker P 2004 A novel computer vision technique for quantitative, objective echocardiographic motion measurement independent of Doppler: first clinical description and validation *Circulation* **110** 3093–99

Sutherland G R, Stewart M J, Groundstroem K W, Moran C M, Fleming A, Guell-Peris F J, Riemersma R A, Fenn L N, Fox K A and McDicken W N 1994 Color Doppler myocardial imaging: a new technique for the assessment of myocardial function *J. Am. Soc. Echocardiogr.* **7** 441–58

Varghese T, Zagzebski J, Rahko P and Breburda C 2003 Ultrasonic imaging of myocardial strain using cardiac elastography *Ultrason. Imaging* **25** 1–16

Villarreal F J, Lew W Y W, Waldman L K and Covell J W 1991 Transmural myocardial deformation in the ischemic canine left-ventricle *Circ. Res.* **68** 368–81

Wang S, Lee W-N, Provost J, Luo J and Konofagou E E 2008 A composite high-frame-rate system for clinical cardiovascular imaging *IEEE Trans. Ultrason. Ferroelectr. Freq. Control* **55** 2221–33

Zervantonakis I K, Fung-Kee-Fung S D, Lee W-N and Konofagou E E 2007 A novel, view-independent method for strain mapping in myocardial elastography: eliminating angle- and centroid-dependence *Phys. Med. Biol.* **52** 4063–80